Multifunctional Carbon-Based Metal-Free Electrocatalysts for Simultaneous Oxygen Reduction, Oxygen Evolution, and Hydrogen Evolution

*Chuangang Hu and Liming Dai**

The ever increasing detrimental effects of traditional fuels on energy and the environment have stimulated extensive efforts worldwide to develop green and renewable energy technologies, including fuel cells,[1] metal–air batteries,[2] and water splitting systems.[3] While the oxygen reduction reaction (ORR) is at the heart of fuel cells, the oxygen evolution reaction (OER) and hydrogen evolution reaction (HER) are of paramount importance to metal–air batteries and electrochemical water-splitting systems.[1a] Catalysts are required for ORR, OER, and HER. Platinum-based noble metal catalysts have been known to be very efficient for ORR and HER whereas Ir- and Ru-based oxides are highly active toward the OER. However, the high cost and limited reserve of these precious metal-based catalysts have precluded the renewable energy technologies from commercialization.[4] To reduce the usage or even to eliminate the precious metal-based catalysts, considerable efforts have been made to develop non-noble metal catalysts for ORR, OER, or HER. In particular, three-dimensional (3D) transition metal (such as Fe, Co, and Ni) sulfides, selenides, nitrides, carbides, phosphides, borides, oxides, hydro(oxy)oxides, and their alloys or complexes have been demonstrated as promising ORR, OER, or HER catalysts.[5] So far, however, most of the nonprecious metal catalysts still remain too expensive for large-scale applications or their catalytic activities are still too low when compared with noble metal catalysts.

On the other hand, catalysts for different reactions (e.g., ORR, OER, or HER) are usually active and stable at different pH values,[1a,3b] which makes the development of integrated energy systems for practical application difficult, if not impossible. Currently, available ORR and OER electrocatalysts often show better performance in an alkaline medium than acidic electrolyte. Due to the inefficient dissociation of water to initiate the Volmer reaction in alkaline electrolytes;[6] however, most HER electrocatalysts exhibit better performance in an acidic medium than alkaline electrolyte, as exemplified by a few-cycle operation lifetime for MoS_2 in alkaline electrolytes.[7] This poses a potential problem when HER is coupled with OER in an overall water splitting process. Therefore, it is highly desirable to develop low-cost, earth-abundant tri-functional electrocatalysts to promote the ORR, OER, and HER simultaneously under the same pH environment.

Along with the intensive research efforts in developing non-precious metal catalysts, carbon-based metal-free catalysts were discovered and have received enormous interest in recent years as they possess combined advantages of low cost, high efficient, long lifetime, and multifunctionality.[8] Rational design of carbon structures with multicomponent active centers can in principle lead to multifunctional catalysts for the ORR, OER, and HER (i.e., tri-functional metal-free catalysts). Herein, we report the development of two-dimensional (2D) N, S co-doped graphitic sheets with a unique hierarchical structure consisting of stereoscopic holes over the graphitic surface (SHG, cf. **Figure 1**a). The presence of SHG ensures a high surface area with abundant interfacial active sites for electrochemical reactions.[1a,9] Previous studies demonstrated that heteroatom-doping of the SHG with nitrogen and sulfur atoms could modulate their electronic and chemical characteristics to further impart functionalities.[1a,8] The abundant accessible active sites coupled with efficient pathways for electron and electrolyte/reactant transports make the newly developed SHG an efficient metal-free ORR/OER/HER tri-functional catalyst with long-term stability in alkaline electrolytes (e.g., 0.1 M KOH). The SHG exhibited an ORR half-wave potential comparable to that of the commercial Pt/C (20% Pt on Vulcan XC-72R; E-TEK), and also showed a comparable OER activity to RuO_2 nanoparticles with a reasonably good HER activity. In this study, SHG was further demonstrated to be one of the best OER and HER bifunctional catalysts for the overall water splitting. This study opens a new avenue for the development of low-cost carbon-based metal-free catalysts to replace noble metals for a large variety of applications, ranging from fuel cells through metal–air batteries to water splitting devices.

The preparation procedures for SHG are depicted in Figure 1a (see also, Figures S1–S7 in the Supporting Information). Briefly, a uniformly formed melamine–nickel sulfate complex was first collected by lyophilization in powder form, which was then mixed well with potassium chloride by ball milling. Thereafter, the resultant powder was annealed at 700 °C for 2 h, followed by heating up to 800 °C with a ramp rate of 6 °C min^{-1} and kept for 2 h under Ar, leading to the N, S co-doped graphitic sheets grown from the Ni and KCl seeds (Figure S1 and Figures S5–S7, Supporting Information, designated as Ni–KCl@SHG). Herein, Ni_2SO_4 was specifically selected as the nickel and sulfur precursors,[9a] and melamine as the carbon and nitrogen source. KCl and KCl coated Ni precursor could serve as the templates for the in situ growth of stereoscopic

Dr. C. Hu, Prof. Dr. L. Dai
Center of Advanced Science and Engineering for Carbon (Case 4carbon)
Department of Macromolecular Science and Engineering
Case Western Reserve University
10900 Euclid Avenue, Cleveland, OH 44106, USA
E-mail: liming.dai@case.edu

DOI: 10.1002/adma.201604942

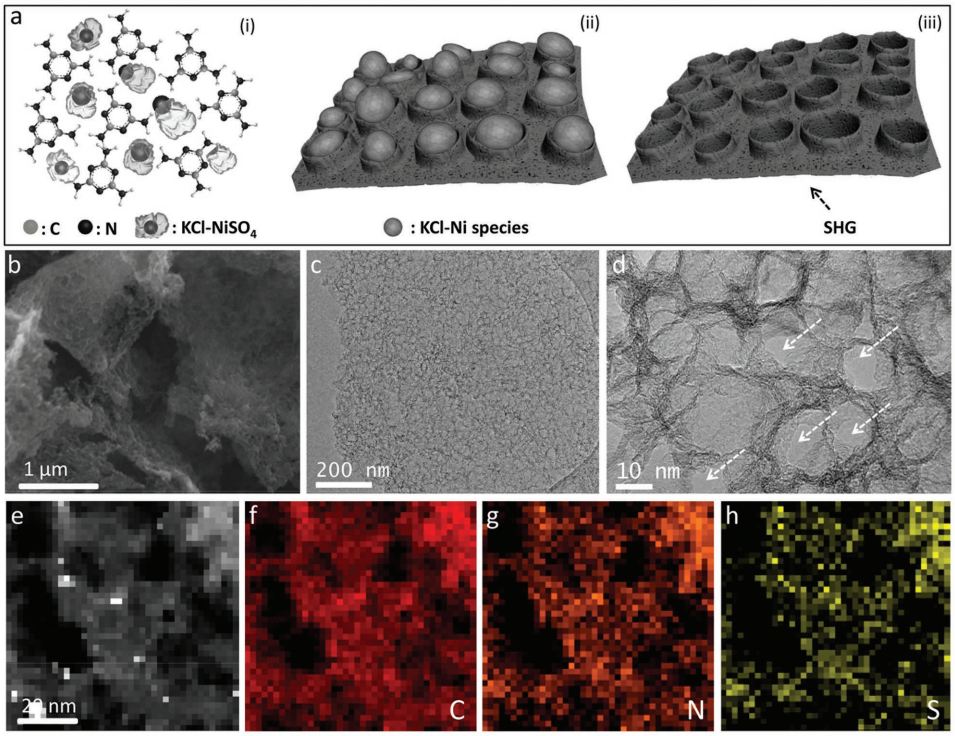

Figure 1. a) Schematic illustration of the preparation process for the SHG. (i) Melamine–nickel sulfate complex mixed well with KCl by ball milling the powder of a melamine–nickel sulfate complex and KCl. (ii) The Ni-KCl@SHG in situ grown from Ni@KCl and KCl seeds were obtained by an annealing process. For clarity, only a piece of the 2D Ni-KCl@SHG is shown. (iii) The structurally well-defined SHG was obtained by etching the Ni@KCl and KCl seeds, followed by additional thermal annealing. b) SEM image of SHG. c,d) TEM images under different magnifications. e) The corresponding HAADF-STEM image of SHG. f–h) EDS mapping images of C, N, and S elements of (e).

holes (Figure 1a) while KCl can also facilitate the graphitization and the formation of catalytic active sites.[10] The nickel and KCl residues were removed by treating with an aqua-regia solution, followed by repeatedly washing with deionized water and lyophilization. Subsequent annealing at 900 °C for 1 h under Ar led to highly conducting (22 S cm^{-1}) N, S co-doped graphitic sheets with stereoscopic holes (SHG, Figure 1b–h).

As reference, separated graphite capsules without a continuous 2D structure and N, S co-doped graphitic sheets without stereoscopic holes, respectively, were prepared under the same conditions with different ratios of melamine to $NiSO_4$. The corresponding samples were designated as GC and GS, respectively (for more details, see Figures S8–S13 in the Supporting Information, and associated discussions in the Supporting Information).

Scanning electron microscopy (SEM) and transmission electron microscopy (TEM) images given in Figure 1b,c and Figures S14–S16 in the Supporting Information, clearly show the 2D structure with a large size of several micrometers for the SHG even after leaching the particles. Enlarged view of the TEM image in Figure 1d reveals that the resultant 2D graphitic sheet was constructed with stereoscopic holes ranging from 5 to 20 nm in diameter. As pointed by arrows in Figure 1d, some opened pores were evident on the 2D graphitic sheets. High-resolution TEM image given in Figure S16 in the Supporting Information shows that edges of the stereoscopic holes are consistent of ≈ 2–4 graphitic layers. Such edge-like graphitic structures could facilitate electrocatalysis. The existence of nanoholes within the SHG sheets was further confirmed by hia gh-angle annular dark-field scanning TEM (HAADF-STEM) image (Figure 1e). As shown by the HAADF-STEM mapping (Figure 1f–h), C, N, and S elements uniformly dispersed over the whole graphitic sheet. The observed highly porous 3D network could provide numerous accessible active sites and rich mesoporosities for effective electron and electrolyte transports necessary for efficient electrocatalysis.

Figure 2a shows the Raman spectrum of SHG. The G-band at 1569 cm^{-1} is associated with the E_{2g} mode, while the D-band located at 1341 cm^{-1} corresponds to the defect mode.[11] The high graphitization degree of the SHG is evident from the high ratio of G-band/D-band (1.29), leading to an improved electrical conductivity. The corresponding X-ray diffraction pattern (Figure S17, Supporting Information) shows two representative peaks at $2\theta \approx 22.3$ and 25.6° attributable to the (002) diffraction plane of graphite (JCPDS 26-0441 and 41-1487).[12] As expected, the energy dispersive spectroscopy (EDS) of SHG reveals the presence of C, N, O, and S elements (Figure 2b), which is confirmed by X-ray photoelectron spectroscopic (XPS) measurements. The observed C, N (2.1 at%) elements are from the melamine precursor and S (0.8 at%) element from $NiSO_4$, along with an O (3.8 at%) peak (Figure S18, Supporting Information), which is common in carbon-based materials.[13] Figure S19 in the Supporting Information shows the high-resolution XPS (HR-XPS) C 1s spectrum, which

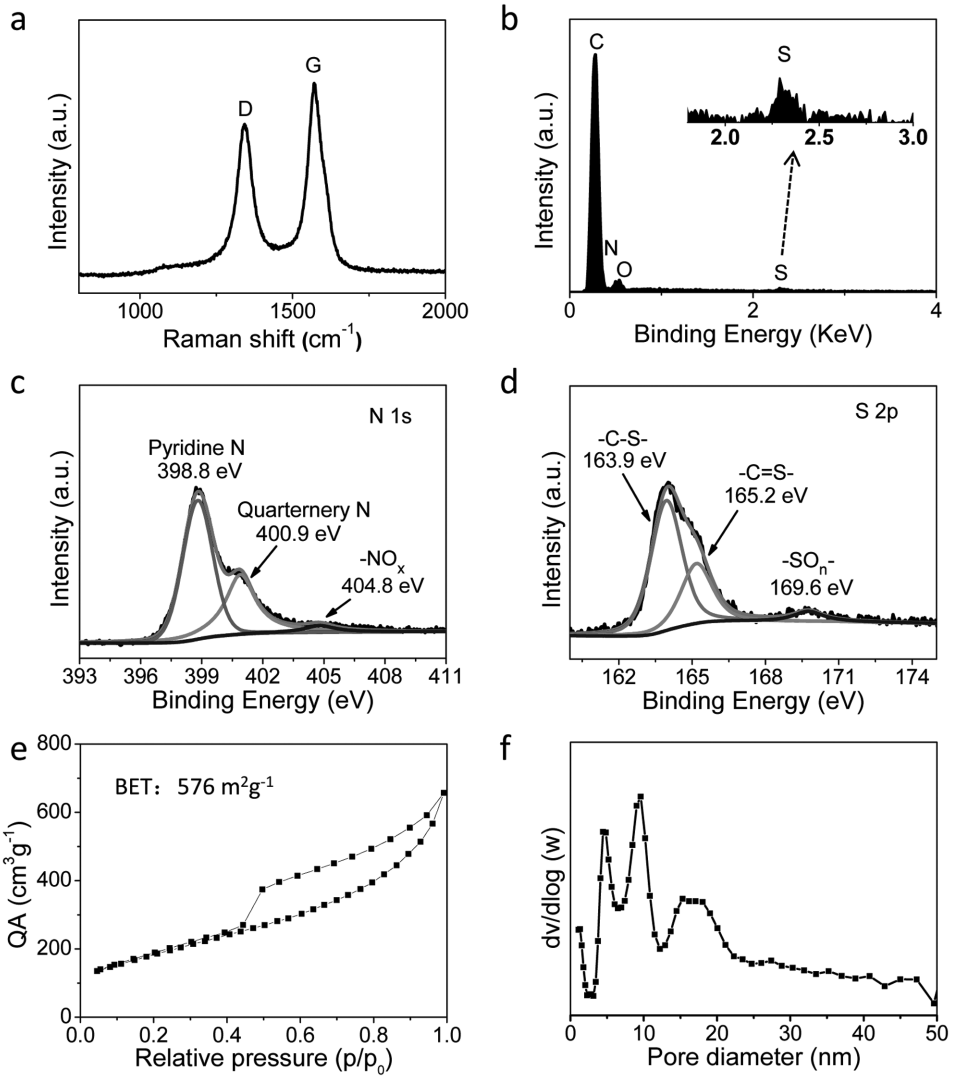

Figure 2. a) Raman spectrum. b) The corresponding EDS spectrum. c,d) HR-XPS of N 1s and S 2p, respectively. Nitrogen adsorption/desorption isotherms (e) and related pore size distribution (f) of SHG.

can be deconvoluted into four peaks corresponding to the typical "C—C/C=C" (284.7 eV), "C—O" (286.3 eV),[12] "C—N" (285.5 eV),[14] and "C—S—C" (284.0 eV)[15] bonds. The successful incorporation of N, S heteroatoms into the carbon backbone was also confirmed by the high-resolution HR-XPS in Figure 2c,d.[9,13] As shown in Figure 2c, two main peaks positioned at 398.8 and 400.9 eV can be identified for pyridinic N and quaternary N, respectively.[9a,16,17] Similarly, the HR-XPS S 2p spectrum can be deconvoluted into two predominate peaks at 163.9 (—C—S—C—) and 165.2 eV (—C=S—)[15,18] (Figure 2d), suggesting the successful doping of S heteroatoms into the carbon skeleton through thermal annealing.[19] The Brunaue–Emmett–Teller specific surface area of the SHG was measured to be 576 m^2 g^{-1} (Figure 2e), which is higher than the corresponding typical values for N-doped CNTs (100 m^2 g^{-1})[20] and graphene materials from pyrolysis of N-rich polymers (200–560 m^2 g^{-1}).[21] The type IV isotherm curve with an obvious hysteresis confirms the presence of mesopores. The rapid N_2 uptake ($P/P_0 > 0.9$) is attributable to the existence of secondary, much larger pores. Barrett–Joyner–Halenda pore size distribution curves derived from the N_2 desorption confirm the presence of the main mesopores with diameters between 3 and 30 nm (Figure 2f) and a pore volume of 1.40 cm^3 g^{-1}. Clearly, therefore, the SHG sample with stereoscopic holes possesses a large surface area, high pore volume, and wide pore size distribution for facilitating the electrocatalysis.

To investigate electrocatalytic performance of the SHG, we firstly carried out cyclic voltammetry (CV) measurements in a conventional three-electrode electrochemical cell in an O_2 or N_2-saturated 0.1 M aqueous KOH solution. As shown in **Figure 3**a, a characteristic oxygen reduction peak at ≈0.88 V was observed for the SHG in O_2-saturated 0.1 M aqueous KOH, but not for the N_2-saturated electrolyte, indicating a high ORR activity for the SHG. We have further performed the linear sweep voltammogram (LSV) measurements on the SHG, GC, and GS samples using a rotating disk electrode (RDE) at

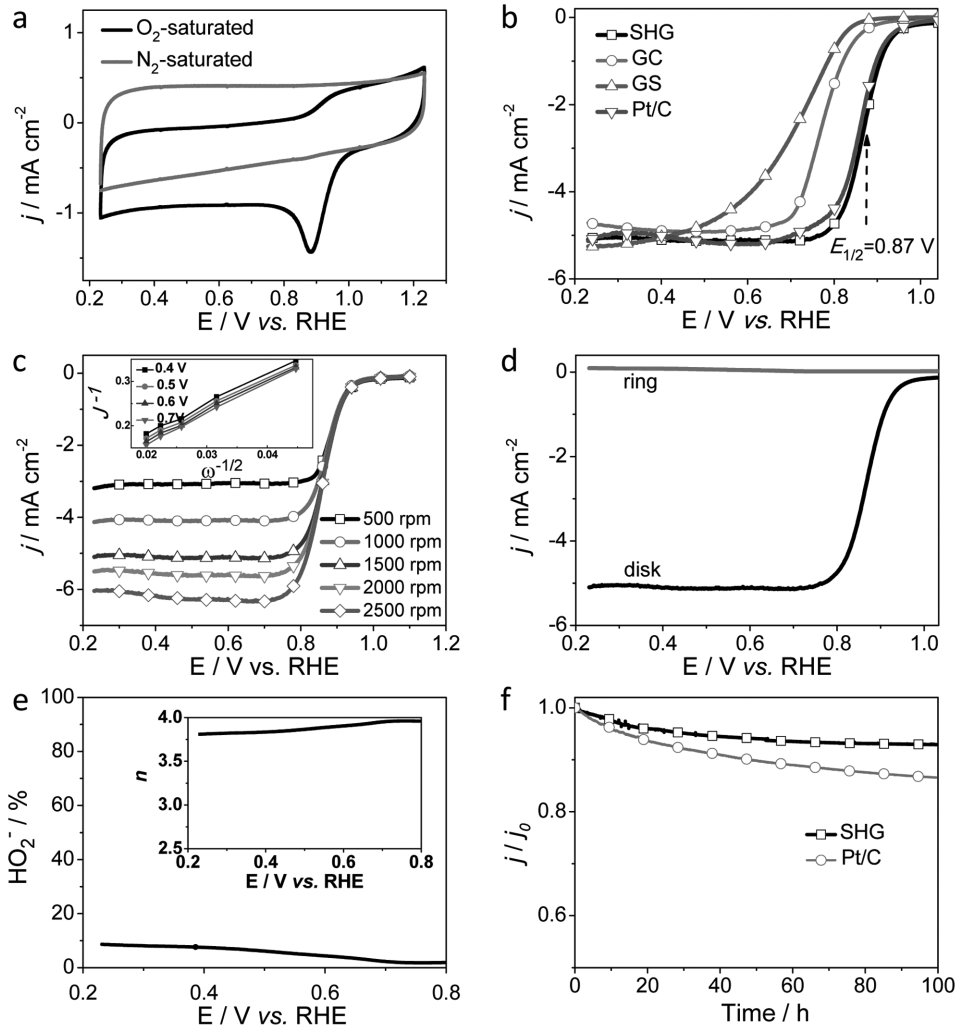

Figure 3. a) CVs of SHG in an O_2 and N_2-saturated KOH solution (0.1 M). b) LSVs on RDE at 1500 rpm. c) LSVs for SHG at various rotating speeds. The inset in (c) shows *K–L* plots obtained from LSVs at different potentials. d) RRDE voltammograms for the SHG at 1500 rpm and the ring electrode was polarized at 1.5 V. The scan rate: 10 mV s^{-1}. e) Peroxide percentage (%H_2O^-) as a function of the electrode potential for SHG at 1500 rpm. The inset in (e) is the corresponding *n* as a function of the electrode potential. f) Current–time chronoamperometric response of SHG and Pt/C in an O_2-saturated KOH solution at a potential of 0.7 V. The rotating speed: 400 rpm. All the potentials were referred to the reversible hydrogen electrode (RHE).

1500 rpm. As seen in Figure 3b, the SHG exhibited similar onset potential (≈ 1.01 V), diffusion-limited current density (≈ 5.10 mA cm^{-2}), and half-wave potential ($E_{1/2}$, ≈0.87 V) as those of the Pt/C catalyst, indicating comparable activities for both catalysts. Compared with many previously reported carbon-based or carbon-supported catalysts (Table S1, Supporting Information), the SHG catalyst exhibited a positive shift in the onset potential, indicating a superior ORR performance. As expected, an increased current with increasing rotation speed was observed (Figure 3c).[9a] Koutecky–Levich (*K–L*) plots (J^{-1}vs $\omega^{-1/2}$) from LSVs given in the inset of Figure 3c show a good linearity with a value of 3.85 for electron transfer (*n*) (Equation (S1), Supporting Information), confirming a four-electron pathway.

To monitor the amount of H_2O_2 generated during the ORR process, a rotating ring-disk electrode (RRDE) technique was employed. Figure 3d shows the disk and ring currents on an RRDE at 1500 rpm. As can be seen, the SHG electrode showed a high limited current density from ORR whereas the current density associated with H_2O_2 oxidation obtained on the Pt-ring was below 10% (Equation (S2), Supporting Information, Figure 3e). The corresponding values for *n* calculated from RRDE voltammograms are between 3.81 and 3.96 (the inset in Figure 3e, Equation (S3) in the Supporting Information), in good agreement with the corresponding data obtained from the *K–L* plots (the inset in Figure 3c). Furthermore, Figure 3f shows only 7% current reduction for the SHG catalyst after a 100 h chronoamperometric test while more than 13% of its initial activity was lost for the Pt/C catalyst under the same condition (0.7 V with O_2 continuous flow in 0.1 M KOH), indicating a higher ORR stability for the SHG than that of the commercial Pt/C.

To further demonstrate the potential application of SHG as a bifunctional catalyst for both ORR and OER, we measured the

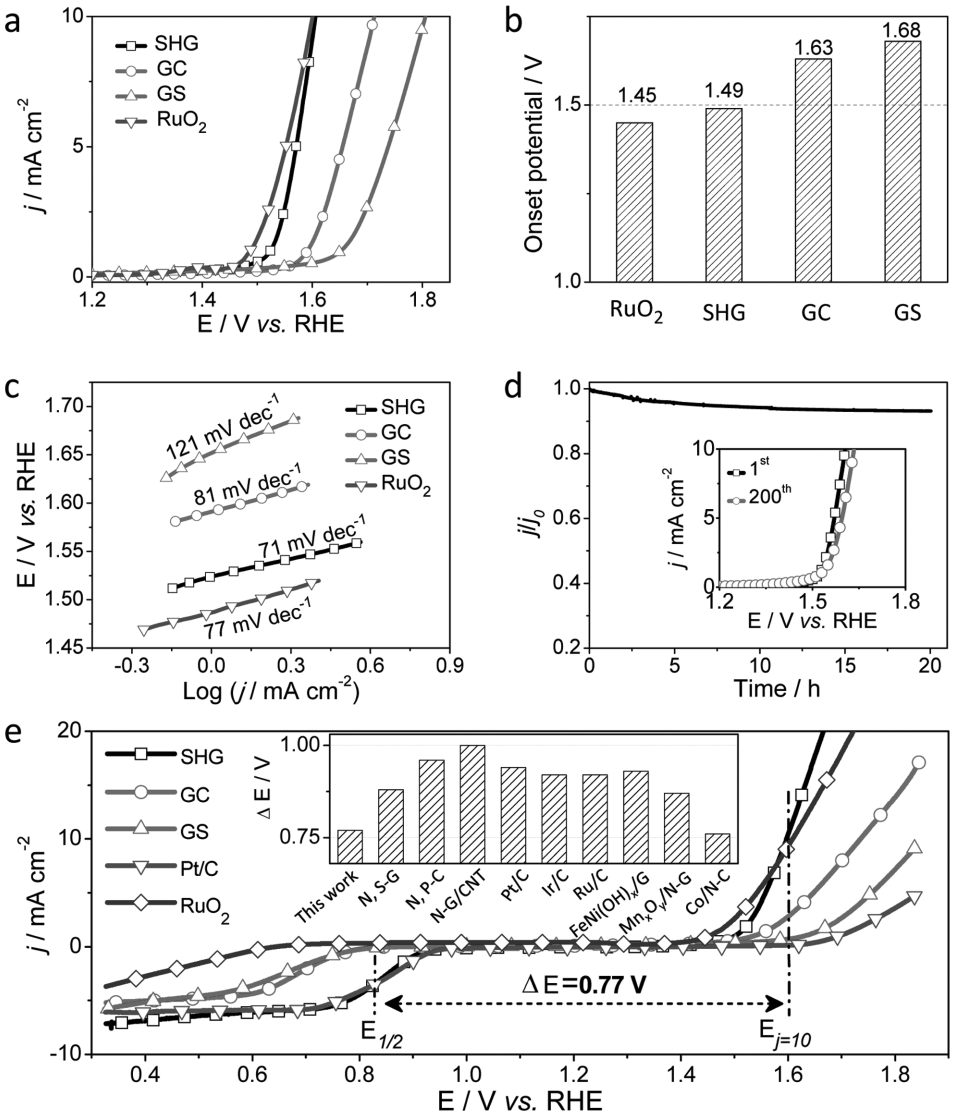

Figure 4. a) Comparison of the OER activity of SHG with GC, GS, and RuO_2 nanoparticles. b) Comparison of the onset potentials of various catalysts (SHG, GC, GS, and RuO_2 nanoparticles). c) Corresponding Tafel plots of these catalysts. d) Chronoamperometric response of SHG at 1.55 V; the insert in (d) LSV plots for the 1st and 200th potential cycles. e) Bifunctional catalytic activities of various catalysts toward both ORR and OER. The overall LSV curves in the potential range of 0.32 to 1.62 V, ΔE ($E_{j=10} - E_{1/2}$) isometric for bifunctional ORR and OER activities, the rotating speed is 1500 rpm. Inset: the values of ΔE for SHG and various catalysts reported previously (see text).

SHG by sweeping the RDE potential between 1.2 and 1.8 V in a 0.1 M KOH electrolyte. The LSV curves thus obtained are reproduced in **Figure 4**a. Compared to the GC and GS electrodes, the SHG electrode exhibited the highest catalytic activity for OER in the alkaline medium. More specifically, the SHG electrode showed the smallest onset potential of 1.49 V (Figure 4b, 1.63 V for GC and 1.68 V for GS), a value which is comparable to that of the RuO_2 catalyst (1.45 V). The SHG electrode showed a potential of 1.56 V at the current of 10.0 mA cm^{-2} (i.e., $E_{j=10}$), which is lower than that of GC (1.71 V) and GS (1.80 V) and many other carbon-based materials (Table S2, Supporting Information). Tafel plots given in Figure 4c display a lower Tafel slope of 71 mV dec^{-1} for the SHG than those of the GC (81 mV dec^{-1}) and GS (121 mV dec^{-1}), indicating more favorable kinetics toward OER on the SHG electrode.[22] This value of 71 mV dec^{-1} is even lower than that of the state-of-the-art RuO_2 (77 mV dec^{-1}). Furthermore, the SHG catalyst showed an excellent stability with an only 7% reduction in the current density of its initial activity after 20 h operation (Figure 4d). The good stability was further confirmed by the similar LSV curves measured at the 1st and 200th potential cycles (the insert in Figure 4d). The overall oxygen activity of the SHG as a bifunctional catalyst can be evaluated by the potential difference (ΔE) between the $E_{j=10}$ for OER and $E_{1/2}$ for ORR with the smaller ΔE for the better reversible oxygen electrode.[9b] Remarkably, the SHG exhibited a ΔE of 0.77 V (Figure 4e), which is much lower than that of most other carbon-based metal-free materials (e.g., N, S-G, ΔE = 0.88; N, P-carbon paper, ΔE = 0.96; N-graphene/CNT, ΔE = 1.00 V),[9b,23]

even outperformed some commercial metal electrocatalysts (e.g., Pt/C, $\Delta E = 0.94$ V; Ir/C, $\Delta E = 0.92$ V; Ru/C, $\Delta E = 0.92$ V),[24] and transition-metals (e.g., FeNi hydroxide/3D graphene, $\Delta E = 0.93$ V; CoO/N-G, $\Delta E = 0.76$ V; Mn_xO_y, $\Delta E = 0.87$ V),[24a,25] as shown in the inset in Figure 4e. These results indicate that the SHG is a promising low-cost, efficient bifunctional catalyst for both ORR and OER simultaneously. From the XPS analysis (Figure 2c,d, Figures S10 and S13, Supporting Information), the S contents in GC and GS samples are relatively low compared with that of SHG. Although GS has a higher N content than that of SHG, its performance is still lower than that of SHG, indicating N, S-codoping is important for the superior activity of SHG. On the other hand, the electrochemical impedance spectroscopic data given in Figure S20 in the Supporting Information revealed that the SHG, compared with the GC and GS, possesses relatively low resistances for electron or ion transports, facilitating the electrochemical processes.

In addition, the HER activities of the SHG were investigated in N_2-saturated KOH electrolyte (0.1 M) using a three-electrode setup. For comparison, we have also recorded the steady-state polarization curves for the GC, GS, Pt/C, and glass carbon, respectively. As shown in **Figure 5**a, all the catalysts exhibited enhanced catalytic activity compared with the glass carbon. In particular, the SHG showed an onset overpotential of ≈230 mV, much lower than those of the GC (290 mV) and GS (380 mV) catalysts. Although the SHG exhibited a more negative onset potential than that of the Pt/C, its absolute value is still much lower than those for other carbon-based materials (Table S3, Supporting Information) and even comparable to some of the well-known non-noble metal HER catalysts in alkaline media (e.g., Ni),[26] indicating a remarkable HER activity for the SHG. The corresponding Tafel plots are given in Figure 5b, which show a lower Tafel slope (112 mV decade^{-1}) for the SHG than those of GC (226 mV decade^{-1}) and GS (240 mV decade^{-1}),

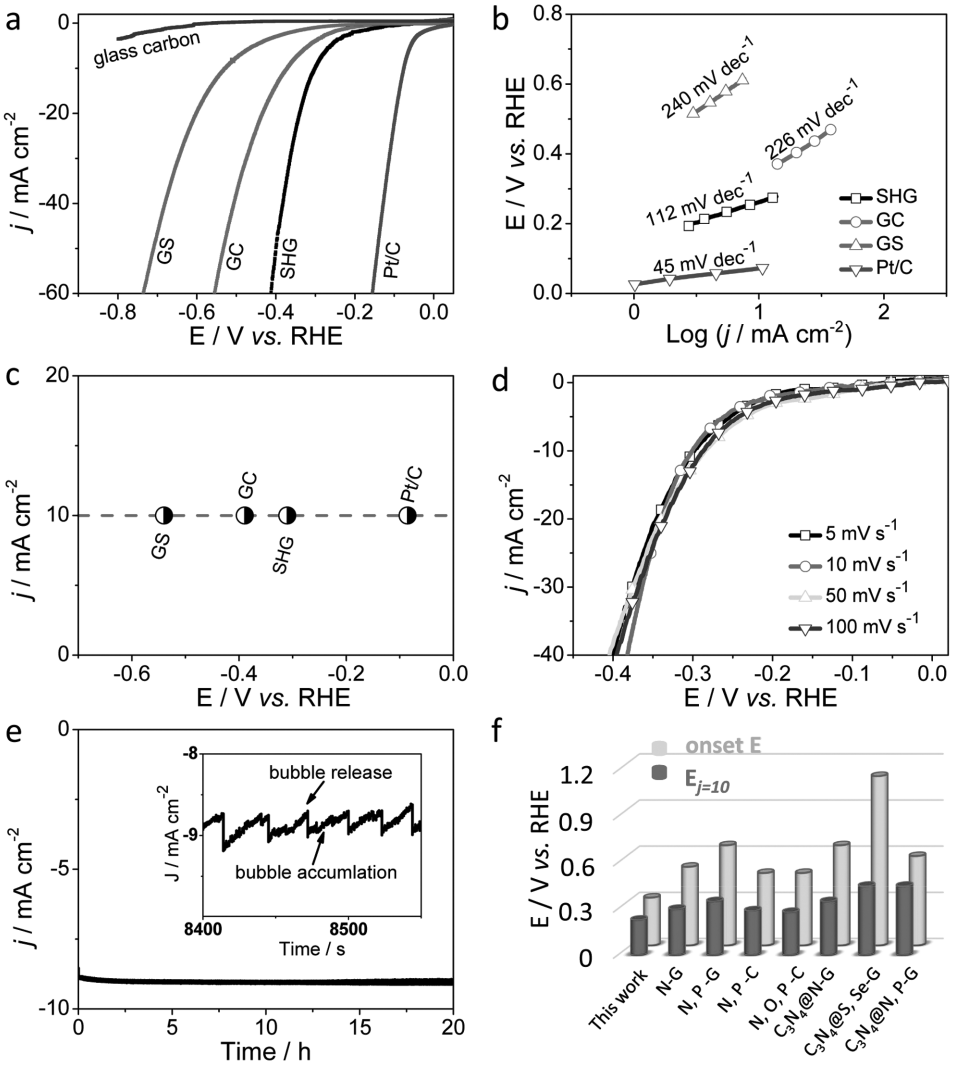

Figure 5. a,b) LSVs and Tafel curves of SHG, GC, GS, 20% Pt/C catalysts, and glass carbon in N_2-saturated 0.1 M KOH solution at a scan rate of 10 mV s^{-1}. c) The HER current density at 10 mA cm^{-2} versus potential for various catalysts. d) Polarization curves of corresponding catalysts with scan rates from 5 to 100 mV s^{-1}. e) Time dependence of the current density at –0.3 V. The insert is the enlargement of (e) from 8400 to 8550 s. f) Comparison of the activities (including the onset potentials and $E_{j=10}$) for various carbon-based materials (see also, Table S3 in the Supporting Information).

suggesting that the release of molecular hydrogen on the SHG is the rate-limiting step.[6a] The overpotentials to achieve the current density of 10 mA cm^{-2} (Figure 5c) for the SHG, GS, GC, and Pt/C are –0.31, –0.39, –0.54, and –0.09 V, respectively. Figure 5d shows similar LSVs at scan rates from 5 to 100 mV s^{-1} for the SHG, demonstrating its excellent stability for highly active electrochemical process. Continuous HER at a given potential was conducted to investigate the durability of the SHG catalyst. As shown in Figure 5e and its insert, a typical serrate shape was observed for the SHG at an overpotential of –0.3 V because of the alternate accumulation and release of H_2 (g) bubbles. The current density is stable without degradation even after long-term cycling for 20 h. Figure S21 in the Supporting Information displays the polarization curves for the SHG electrode before and after the continuous HER process (20 h), showing only a slight deactivation of the activity on the SHG electrode. Overall, the SHG catalyst exhibited a low onset potential, high current density, and long-term stability, promising for HER in alkaline medium. As presented in Table S3 in the Supporting Information, the onset potential and $E_{j=10}$ value of the SHG electrode are the lowest among all the carbon-based materials, including N-doped graphene (N-G);[27] N, P-graphene (N, P-G);[28] N, P-carbon network (N, P-C);[29] N, O, P tri-doped porous carbon (N, O, P-C);[30] g-C_3N_4@N-doped graphene (C_3N_4@G);[6a] g-C_3N_4–S, Se co-doped graphene (C_3N_4@S, Se-G);[31] and g-C_3N_4-N, P co-doped graphene (C_3N_4@N, P-G).[32]

Since the SHG has been demonstrated to be an active and stable bifunctional catalyst toward both OER and HER, we constructed a two electrode setup, in which the SHG was used as both anode and cathode, for electrochemical water splitting in 1 M KOH. As seen in **Figure 6**a, the SHG HER electrode (with the same SHG as the OER counter electrode) shows a small onset potential of –250 mV with the current density gradually increased with increasing potential, as is the case for the Pt/C and RuO_2 setup. In conjunction with the other half reaction for OER (Figure 6b), the galvanostatic cycling method demonstrated an attractive two electrode water-splitting process based

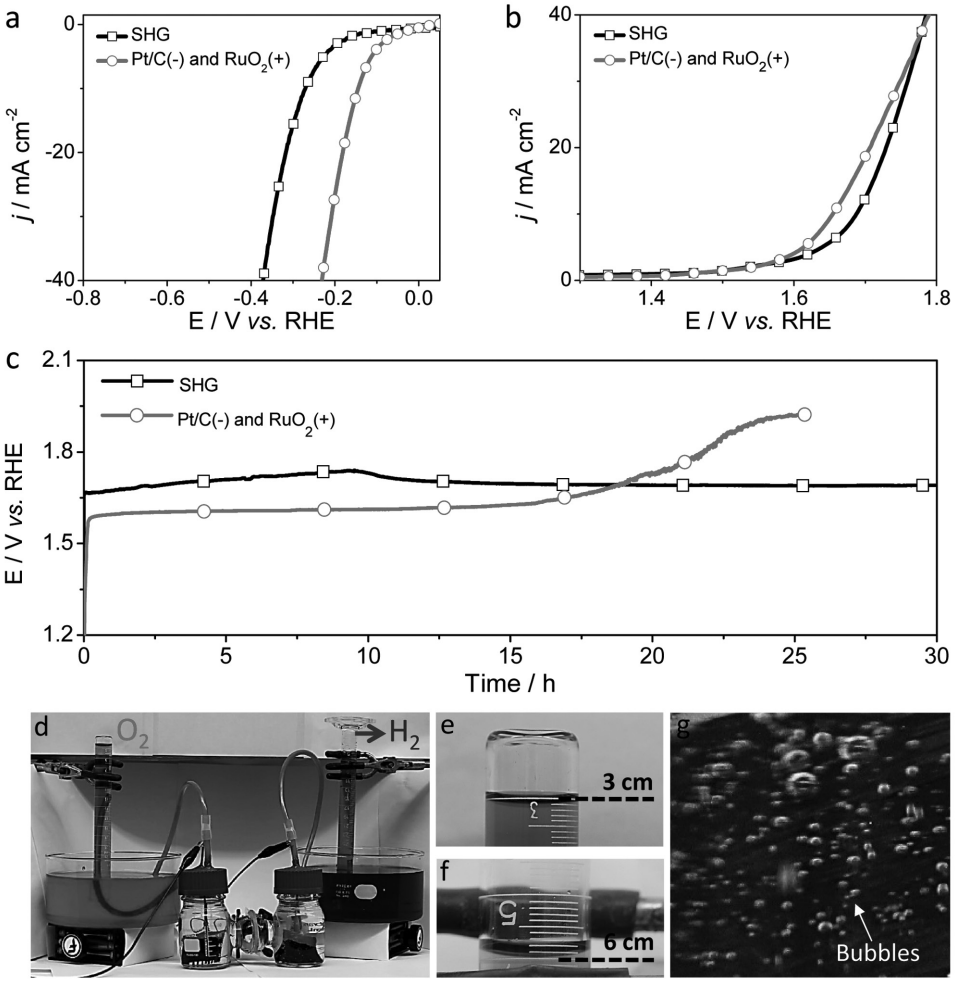

Figure 6. a) HER and b) OER activities of SHG(–)/SHG(+) and Pt/C(–)/RuO_2(+) two-electrode setup with the scan rate of 10 mV s^{-1}; the electrolyte: 1.0 M KOH. c) Chronopotentiometric curve of water electrolysis for SHG(–)/SHG(+) and Pt/C(–)/RuO_2(+) with constant current density of 10 mA cm^{-2} in 1.0 M KOH. d) The demononstration of SHG in a homemade two-electrode water splitting device by chronopotentiometry at a given potential of 2 V. The carbon fiber woven mesh (3 × 2 cm) was used as an all-carbon electrode for deposition the SHG catalyst. e) Oxygen and f) hydrogen collection process with displacement of water. g) Bubbles generated from the electrode (e.g., H_2 electrode) during the water splitting process.

on the SHG bifunctional catalyst with compatible performance to its counterpart based on the Pt and RuO_2 for HER and OER catalyst, respectively. The overall water splitting polarization of the SHG-based cell exhibited a slightly larger onset voltage than that of the Pt/C(–)/RuO_2(+) benchmark combination, but quickly approaching the same due to the facile kinetic and bubble-releasing processes (Figure 6c). The voltage to achieve the 10 mA cm^{-2} electrolysis current showed a self-activation process; a potential of 1.70 V was required to deliver 10 mA cm^{-2} at the initial stage, followed by a stable ≈1.68 V for continuous operation (Figure 6c) with a vigorous gas evolution on both electrodes, outperforming the Pt/RuO_2 combination after 19 h operation. Although the RuO_2 and Pt/C combination showed an efficient starting voltage, it was followed by rapid decay. The stable potential ≈1.68 V based on the SHG electrodes is similar or lower than the corresponding value for many previously reported non-noble metal based catalysts, including diselenides (NiSe/NF, 1.63 V),[33] hydroxides (NiFe LDH/NF, 1.7 V),[34] and cobalt sulfide/carbon tube (1.74 V).[35] Figure 6d and Figure S22 in the Supporting Information display the homemade two-electrode water splitting device based on the carbon-fiber-woven mesh electrode (3 × 2 cm) pre-coated with the SHG catalyst (Figure S23, Supporting Information). H_2 and O_2 thus generated were collected by displacement of water methods (Figure 6e,f, see, Supporting Information for detailed description), and the Faradaic efficiency of the two-electrode setup was demonstrated to be close to 100% for overall water splitting with the volume ratio of H_2 and O_2 approaching to the theoretical value of 2:1 during the electrolysis. Due to the appropriate surface hydrophobicity (Figure S24, Supporting Information), bubbles generated from the carbon fiber electrode (e.g., H_2 electrode) during the water splitting process could easily leave from the electrode surface (Figure 6g, Movie S1, Supporting Information) to ensure long-term stability. Superior to both GC and GS, SHG was found to also show good ORR, OER, and HER performance in acid solution and neutral media (see, Figures S25 and S26 in the Supporting Information). As expected, the electrochemical behavior of the SHG was also found to be affected by its structure, composition, and conductivity (Figures S27–S38, Supporting Information). Generally speaking, water oxidation involves the following three intermediate steps: water adsorption, water dissociation, and oxygen evolution. Our results indicate that a number of the N and S elements on the SHG catalyst generate "C^+" centers[1c] to promote the water adsorption while the large surface area and holey structure facilitate mass transport, electron transfer, and ion diffusion within the electrode for efficient water splitting.

In this study, we have prepared 2D N, S co-doped graphitic sheets with a unique hierarchical structure consisting of stereoscopic holes over the graphitic surface (SHG). The presence of stereoscopic holes in SHG ensures a high surface area with abundant interfacial active sites for electrochemical reactions. Owing to its unique architecture with a large surface area, rich active sites, and good electron/electrolyte transport properties, the newly developed SHG was demonstrated to be an effective tri-functional ORR/OER/HER catalyst of excellent activities and stability, outperformed its counterparts without opened holes or continuous 2D structure as well as many other carbon materials. This, together with its low cost and facile synthesis, makes the SHG a promising alternative to noble metal based catalysts for fuel cells, metal–air batteries, water splitting and many other applications.

Supporting Information

Supporting Information is available from the Wiley Online Library or from the authors.

Acknowledgements

This work was supported by NSF (CMMI-1400274) and AFOSR (FA9550-12-1-0037).

Received: September 13, 2016
Revised: November 8, 2016
Published online:

[1] a) L. M. Dai, Y. H. Xue, L. T. Qu, H.-J. Choi, J.-B. Baek, *Chem. Rev.* **2015**, *115*, 4823; b) C. G. Hu, H. H. Cheng, Y. Zhao, Y. Hu, Y. Liu, L. M. Dai, L. T. Qu, *Adv. Mater.* **2012**, *24*, 5493; c) K. P. Gong, F. Du, Z. H. Xia, M. Durstock, L. M. Dai, *Science* **2009**, *323*, 760.

[2] a) J. T. Zhang, Z. H. Xia, L. M. Dai, *Sci. Adv.* **2015**. *1*, e1500564; b) Q. Li, R. G. Cao, J. Cho, G. Wu, *Adv. Energy Mater.* **2014**, *4*, 1301415; c) J. L. Shui, M. Wang, F. Du, L. M. Dai, *Sci. Adv.* **2015**. *1*, e1400129.

[3] a) H. T. Wang, H.-W. Lee, Y. Deng, Z. Y. Lu, P.-C. Hsu, Y. Y. Liu, D. C. Lin, Y. Cui, *Nat. Commun.* **2015**, *6*, 7261; b) J. H. Wang, W. Cui, Q. Liu, Z. C. Xing, A. M. Asiri, X. P. Sun, *Adv. Mater.* **2016**, *28*, 215.

[4] a) M. Cabán-Acevedo, M. L. Stone, J. R. Schmidt, J. G. Thomas, Q. Ding, H. C. Chang, M. L. Tsai, J. H. He, S. Jin, *Nat. Mater.* **2015**, *14*, 1245; b) J. Q. Tian, Q. Liu, N. Y. Cheng, A. M. Asiri, X. P. Sun, *Angew. Chem.* **2014**, *126*, 9731; *Angew. Chem. Int. Ed.* **2014**, *53*, 9577.

[5] a) X. Long, G. X. Li, Z. L. Wang, H. Y. Zhu, T. Zhang, S. Xiao, W. Y. Guo, S. H. Yang, *J. Am. Chem. Soc.* **2015**, *137*, 11900; b) A. B. Laursen, K. R. Patraju, M. J. Whitaker, M. Retuerto, T. Sarkar, N. Yao, K. V. Ramanujachary, M. Greenblatt, G. C. Dismukes, *Energy Environ. Sci.* **2015**, *8*, 1027; c) E. J. Popczun, C. G. Read, C. W. Roske, N. S. Lewis, R. E. Schaak, *Angew. Chem.* **2014**, *126*, 5531; *Angew. Chem. Int. Ed.* **2014**, *53*, 5427; d) R. D. Smith, M. S. Prévot, R. D. Fagan, Z. Zhang, P. A. Sedach, M. K. J. Siu, S. Trudel, C. P. Berlinguette, *Science* **2013**, *340*, 57.

[6] a) Y. Zheng, Y. Jiao, Y. H. Zhu, L. H. Li, Y. Han, Y. Chen, A. J. Du, M. Jaroniec, S. Z. Qiao, *Nat. Commun.* **2014**, *5*, 3783; b) C. G. Hu, L. M. Dai, *Angew. Chem. Int. Ed.* **2016**, *55*, 2; *Angew. Chem.* **2016**, *128*, 2.

[7] M. Zeng, Y. G. Li, *J. Mater. Chem. A* **2015**, *3*, 14942.

[8] a) L. M. Dai, *Acc. Chem. Res.* **2013**, *46*, 31; b) D. S. Yu, E. Nagelli, F. Du, L. M. Dai, *J. Phys. Chem. Lett.* **2010**, *1*, 2165; c) Y. Zheng, Y. Jiao, M. Jaroniec, S. Z. Qiao, *Angew. Chem. Int. Ed.* **2015**, *54*, 52; *Angew. Chem.* **2015**, *127*, 52; d) Y. Jiao, Y. Zheng, M. Jaroniec, S. Z. Qiao, *Chem. Soc. Rev.* **2015**, *44*, 2060; e) S. Y. Wang, L. P. Zhang, Z. H. Xia, A. Roy, D. W. Chang, J.-B. Baek, L. M. Dai, *Angew. Chem. Int. Ed.* **2012**, *51*, 4209; *Angew. Chem.* **2012**, *124*, 4285.

[9] a) C. G. Hu, L. X. Wang, Y. Zhao, M. H. Ye, Q. Chen, Z. H. Feng, L. T. Qu, *Nanoscale* **2014**, *6*, 8002; b) S. Chen, J. J. Duan, Y. Zheng, X. M. Chen, X. W. Du, M. Jaronie, S. Z. Qiao, *Energy Storage Mater.*

2015, *1*, 17; c) X. F. Liu, M. Antonietti, *Adv. Mater.* **2013**, *25*, 6284; d) K. G. Qu, Y. Zheng, S. Dai, S. Z. Qiao, *Nano Energy* **2016**, *19*, 373; e) Y. Ito, W. T. Cong, T. Fujita, Z. Tang, M. W. Chen, *Angew. Chem.* **2015**, *12*, 2159; *Angew. Chem. Int. Ed.* **2015**, *54*, 2131; f) X. J. Liu, W. J. Zhou, L. J. Yang, L. G. Li, Z.Y. Zhang, Y. T. Ke, S. W. Che, *J. Mater. Chem. A* **2015**, *3*, 8840.

[10] W. Ding, L. Li, K. Xiong, Y. Wang, W. Li, Y. Nie, S. G. Chen, X. Q. Qi, Z. D. Wei, *J. Am. Chem. Soc.* **2015**, *137*, 5414.

[11] C. G. Hu, L. X. Lv, J. L. Xue, M. H. Ye, L. X. Wang, L. T. Qu, *Chem. Mater.* **2015**, *27*, 5253.

[12] C. G. Hu, X. Q. Zhai, L. L. Liu, Y. Zhao, L. Jiang, L. T. Qu, *Sci. Rep.* **2013**, *3*, 2065.

[13] S. Y. Wang, E. Lyyamperumal, A. Roy, Y. H. Xue, D. S. Yu, L. M. Dai, *Angew. Chem. Int. Ed.* **2011**, *50*, 11756; *Angew. Chem.* **2011**, *123*, 11960, and references cited therein.

[14] a) C. G. Hu, Y. Xiao, Y. Zhao, N. Chen, Z. P. Zhang, M. H. Cao, L. T. Qu, *Nanoscale* **2013**, *5*, 2726; b) L. T. Qu, Y. Liu, J.-B. Baek, L. M. Dai, *ACS Nano* **2010**, *4*, 1321.

[15] J. Liang, Y. Jiao, M. Jaroniec, S. Z. Qiao, *Angew. Chem. Int. Ed.* **2012**, *51*, 11496; *Angew. Chem.* **2012**, *124*, 11664.

[16] S. A. Wohlgemuth, R. J. White, M. G. Willinger, M. M. Titirici, M. Antonietti, *Green Chem.* **2012**, *14*, 1515.

[17] Z. L. Wang, D. Xu, H. G. Wang, Z. Wu, X. B. Zhang, *ACS Nano* **2013**, *7*, 2422.

[18] Z. Yang, Z. Yao, G. F. Li, G. Y. Fang, H. G. Nie, Z. Liu, X. M. Zhou, X. A. Chen, S. M. Huang, *ACS Nano* **2012**, *6*, 205.

[19] J. T. Zhang, Z. H. Zhao, Z. H. Xia, L. M. Dai, *Nat. Technol.* **2015**, *10*, 444.

[20] S. Maldonado, K. J. Stevenson, *J. Phys. Chem. B* **2005**, *109*, 4707.

[21] L. F. Lai, J. R. ZPotts, D. Han, L. Wang, C. K. Poh, C. H. Tang, H. Gong, Z. X. Shen, J. Y. Lin, R. S. Ruoff, *Energy Environ. Sci.* **2012**, *5*, 7936.

[22] B. Y. Xia, Y. Yan, N. Li, H. B. Wu, X. W. Lou, X. Wang, *Nat. Energy* **2016**, *1*, 15006.

[23] a) T. Y. Ma, J. Ran, S. Dai, M. Jaroniec, S. Z. Qiao, *Angew. Chem. Int. Ed.* **2015**, *54*, 4646; *Angew. Chem. Int. Ed.* **2015**, *127*, 4729; b) G.-L. Tian, M.-Q. Zhao, D. Yu, X.-Y. Kong, J.-Q. Huang, Q. Zhang, F. Wei, *Small* **2014**, *10*, 2251.

[24] a) J. Masa, W. Xia, I. Sinev, A. Zhao, Z. Sun, S. Grützke, P. Weide, M. Muhler, W. Schuhmann, *Angew. Chem. Int. Ed.* **2014**, *53*, 8508; *Angew. Chem.* **2014**, *126*, 8648; b) Y. Gorlin, T. F. Jaramillo, *J. Am. Chem. Soc.* **2010**, *132*, 13612.

[25] a) Y. Li, M. J. Zhao, Y. Zhao, L. Song, Z. P. Zhang, *Part. Part. Syst. Charact.* **2016**, *33*, 158; b) S. Mao, Z. H. Wen, T. Z. Huang, Y. Hou, J. H. Chen, *Energy Environ. Sci.* **2014**, *7*, 609.

[26] H. Vrubel, X. Hu, *Angew. Chem.* **2012**, *124*, 12875; *Angew. Chem. Int. Ed.* **2012**, *51*, 12703.

[27] J. M. Ge, B. Zhang, L. B. Lv, H. H. Wang, T. N. Ye, X. Wei, J. Su, K. X. Wang, X. H. Lin, J. S. Chen, *Nano Energy* **2015**, *15*, 567.

[28] Y. Zheng, Y. Jiao, L. H. Li, T. Xing, Y. Chen, M. Jaroniec, S. Z. Qiao, *ACS Nano* **2014**, *8*, 5290.

[29] J. T. Zhang, L. T. Qu, G. Q. Shi, J. Y. Liu, J. F. Chen, L. M. Dai, *Angew. Chem. Int. Ed.* **2016**, *55*, 2230; *Angew. Chem.* **2016**, *128*, 2270.

[30] J. P. Lai, S. P. Li, F. X. Wu, M. Saqib, R. Luque, G. B. Xu, *Energy Environ. Sci.* **2016**, *9*, 1210.

[31] S. S. Shinde, A. Sami, J. H. Lee, *J. Mater. Chem. A* **2015**, *3*, 12810.

[32] S. S. Shinde, A. Sami, J. H. Lee, *ChemCatChem* **2015**, *7*, 3873.

[33] C. Tang, N. Cheng, Z. Pu, W. Xing, X. Sun, *Angew. Chem. Int. Ed.* **2015**, *54*, 9351; *Angew. Chem.* **2015**, *127*, 9483.

[34] J. Luo, J.-H. Im, M. T. Mayer, M. Schreier, M. K. Nazeeruddin, N.-G. Park, S. D. Tilley, H. J. Fan, M. Grätzel, *Science* **2014**, *345*, 1593.

[35] J. Wang, H. X. Zhong, Z. L. Wang, F. L. Meng, X. B. Zhang, *ACS Nano* **2016**, *10*, 2342.